Changes in Larsen B ice shelf dynamics prior to breakup: satellite borne observations and modelling outcomes

Wolfgang Rack and Henner Sandhäger
wrack@awi-bremerhaven.de, hsandhaeger@awi-bremerhaven.de
Alfred Wegener Institute for Polar und Marine Research, Bremerhaven, Germany

Helmut Rott and Claudia Riedl
helmut.rott@uibk.ac.at, c.riedl@uibk.ac.at
Institute for Meteorolgy and Geophysics, University of Innsbruck, Austria

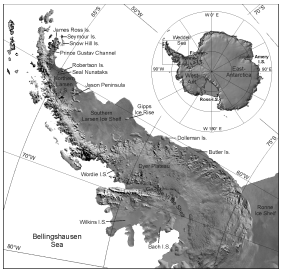

Figure 1: Antarctic Peninsula and location of the Northern Larsen Ice Shelf (NLIS).

The pattern of the final break-up of the northern Larsen B ice shelf in March 2002 was comparable to the collapse of Larsen A in January 1995, although the retreat of Larsen A previous to the collapse was more gradual, extending over a multi-year period. This can be attributed to the different geometry of the confining bay, where Lindenberg Island acted as pinning point delaying the disintegration. For both ice shelf sections, the presence of abundant melt water during summers as a consequence of climate warming is regarded as one of the key factors which increased the vulnerability of the ice shelf. The rapidity of the final disintegration event was fostered by pre-existing rifts along major parts of the grounding zone, along the boundaries to the stagnant ice shelf section at Seal Nunataks, and on major parts of the ice shelf (Rack and Rott, in press). Remote sensing analysis based on ERS and Envisat SAR as well as optical imagery is used to set up boundary conditions for a numerical ice shelf model. This finite-difference model (Sandhäger, 2000; in press) solves the usual continuum-mechanical equations of ice shelf motion, but also considers large-scale influences of fractures on the flow regime.

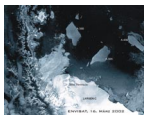

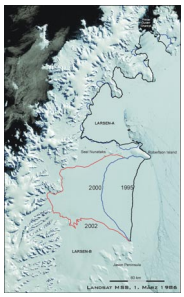

Figure 2: Stages of retreat of the northern Larsen Ice Shelf 1986-2002, derived from optical satellite and SAR images.

See the full image sequence 1986-2002 as movie at: http://dude.uibk.ac.at/Projects/Larsen_Ice_Shelf

SATELLITE BORNE AND GROUND BASED OBSERVATIONS

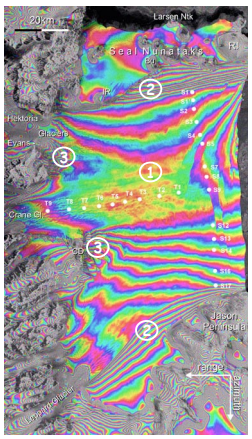

The remote sensing analysis is based on ERS SAR data acquired in the 10 year period between 1992 and 2002. Of major importance is the application of SAR interferometry with data acquired during the ERS-1/2 Tandem mission between 1995 and 1999. Ground control points from field surveys in the central part and along the coast of the embayment are used as reference for the relative interferometric measurements (Fig. 3).

The first interferograms were acquired in 1995, ten month after the calving of the large iceberg A25. Already at this time, the ice shelf was probably out of balance. The northern part of NLIS continued to retreat, whereas the southern part advanced for a few more years. Discontinuities in the fringe pattern show that rifts have formed up to 20 km behind the ice edge, which cut completely through the ice.

Prior to 1995 information on flow behavior is available from field measurements and feature tracking of optical satellite images. Fig. 4 shows several flow lines, manually derived from a Landsat MSS image (1986) and ERS images. In addition, the velocity profile along the central flow line (C) in the late 1980s and in 1995 is displayed. In the central part, the motion profile is almost uniformly shifted to higher values, only near the ice edge strain rates are significantly higher.

Figure 3: ERS SAR interferogram (satellite track 152, 15-16 November 1995) of Larsen B and locations of field measurements between 1996 and 1999.

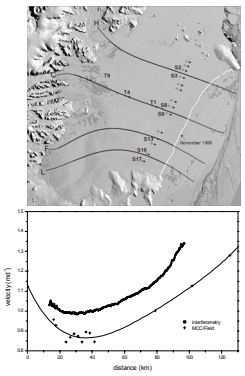

Figure 4: a) Landsat MSS image (1 March 1986), showing major flow lines and points of feature tracking between 1986 and 1988. b) Ice shelf velocity along the central flowline of Crane Glacier before and after 1995, derived by satellite imagery.

Between 1995 and 1999 the deformation pattern in the shear zones changed significantly. Fig. 5 shows the change in flow behavior at the northern shear margin of Larsen B. This part of Larsen B boarders the stagnant ice shelf section of Seal Nunataks. Downstream the ice rise (IR) 2 to 3 more fringes are counted in a narrow zone of about 10 km. This shows that the acceleration is due to higher shear in confined bands at the margin. Several more rifts are visible in the 1999 interferogram. At this time the ice edge had retreated by several more kilometers and the stakes of the northern part of the S-profile were lost.

The acceleration is in accordance to field measurements along the S- and T-profile (Fig. 3,4). It amounts to about 10 ma^{-2} in the central part, 5 ma^{-2} in the north, and 4 ma^{-2} in the south.

Because of warm summers and strong melting, the surface mass balance of the northern part of NLIS became small or even negative in the early 1990s. Large melt water ponds and channels are visible in satellite images. In years with mean summer temperatures well above the long term average the strongest calving events were observed.

The evidence for increased ocean driven melting is small. However, enhanced bottom melting could have occured after the break-up of Larsen A because of a change in water circulation in the sub-ice shelf cavity.

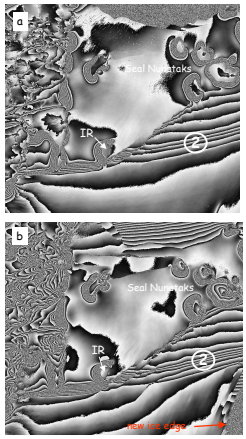

Figure 5: ERS SAR Interferograms (satellite track 424) of the area around Seal Nunataks and the northern shear margin of Larsen B. a) 1995, b) 1999.

ICE SHELF MODELLING

The diagnostic simulations of ice shelf dynamics are performed with a finite-difference model which solves the general governing equations of ice shelf flow. The equations combine the continuum-mechanical momentum and mass balance equations, Glen's flow law and the ice shelf approximation. The enhancement factor of the flow law depends on ice temperature, which is calculated from surface temperature by means of a simple relation (instead of solving the heat transfer equation). Involving boundary conditions, the computation yields ice velocities, strain rates, and stresses, according to the ice shelf geometry.

The main geometrical and ice dynamical input datasets are shown in Fig. 6. The ice thickness distribution is derived from the BEDMAP database (Lythe et al., 2001) and converted elevation data (Bamber and Huybrechts, 1996). Velocities of glacier outflows and grounding line position result from ERS SAR interferometry. Mean annual surface temperatures (inset) are chosen according to measurements at Matienzo Station (MAT; Rack, 2000) and the distribution represented by Vaughan and Doake (1996).

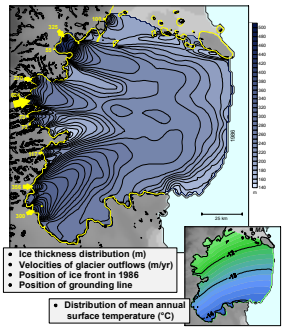

Figure 6: Specification of essential input quantities for the numerical simulations.

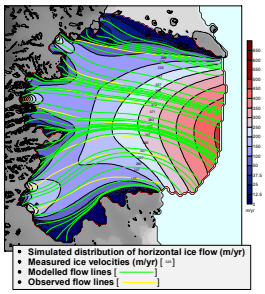

Figure 7: Larsen B flow regime as derived from the reference run using the ordinary ice shelf model. Considerable discrepancies between model results and observations can be ascertained. In particular, the computed ice velocities for the central ice shelf part are too low, and the simulated velocity field for the marginal ice shelf areas is much lesser differentiated in comparison to the real situation (cf., Fig. 3).

Analysing the results of a reference run (Fig. 7) clearly indicates that the ordinary ice shelf model provides an inadequate description of the observed flow regime. This deficiency cannot be explained by uncertainties in the input data alone, but suggests the existence of important ice dynamical processes which remained so far unconsidered.

The concept for model advancement is taken from the observation that pronounced fracture zones cause dynamical decoupling. To consider this process in our model, we developed the numerical approach illustrated in Figure 8. The basic hypothesis is that high shear stress causes fracture zone formation with substantial reductions in both the horizontal shear strain and the ice stiffness.

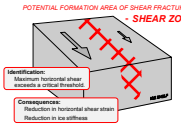

Figure 8: Sketch illustrating the new numerical approach.

The results obtained with the advanced model (Fig. 9) agree considerably better with observations and are essentially more plausible from the glaciological point of view. In particular, the complex structure of the velocity field and the large strain rates in marginal zones are better reproduced.

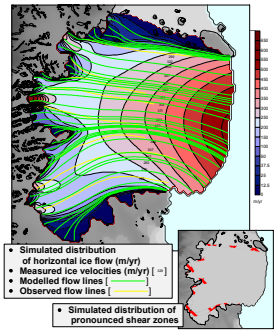

Figure 9: Larsen B flow regime as computed with the advanced ice shelf model. Measured ice velocities and observed flow lines are largely reproduced. The inset indicates areas where shear fracture formation and dynamical decoupling are simulated.

DISCUSSION

To validate the model results we compared the distributions of simulated shear zones and observed surface features (Fig. 10). According to the model results nearly the whole ice shelf area is confined by fracture zones, which is largely confirmed by the optical satellite image. Inconsistency is observed e.g. south of Seal Nunataks and in SCAR inlet, which can be attributed to the simplified model assumptions.

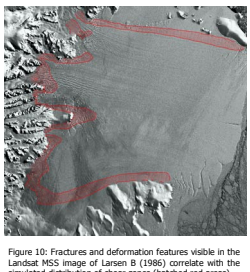

Figure 10: Fractures and deformation features visible in the Landsat MSS image of Larsen B (1986) correlate with the simulated distribution of shear zones (hatched red areas).

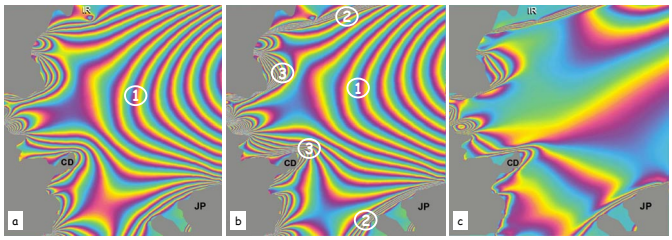

Figure 11: Synthetic interferograms for the model velocities as derived from (a) the reference run and (b) the application of the expanded model; (c) shows the difference of both. Synthetic and real interferograms (Fig. 3 and 5) can be directly compared (see text).

Simulated ice velocities are converted to synthetic interferograms in ERS SAR geometry (Fig. 11), providing a quantitative comparison with the corresponding real interferogram (Fig. 3). In contrast to the observed fringe pattern, the interferograms of both model runs show a high sequence of fringes in the central part (-1-). This means that the flow model overestimates the longitudinal velocity gradient, indicating that the used temperature estimate is to high, and, thus, the calculated ice viscosity is to low.

Apart from this deficiency it is evident that including shear zone simulation significantly improves the model results.

Regarding the typical narrow fringe sequences occuring along the marginal zones (Fig. 3, -2-) and prominent inland parts (-3-), these structures are only reproduced in the synthetic interferogram of the advanced model run. This is particularly revealed by the differential synthetic interferogram (Fig. 11 c).

The fringe pattern -2- and -3- represents zones of large strain and, hence, indicates potential formation areas of crevasses and shear fractures. Taking this into account, an overall consistency between new model approach, model output, ERS SAR interferogram, and observed distribution of surface features can be ascertained.

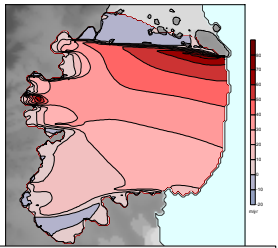

Figure 12: Assessment of the possible impact of shear zone activation, e.g. due to enhanced melt water infiltration.

The advanced ice shelf model is used for a preliminary sensitiviy study. Increased melting due to atmospheric warming is supposed to foster melt water infiltration into fracture zones, leading to enhanced dynamical decoupling. Considering such a scenario, this results in an increase in velocity as shown in Fig. 12. The magnitude of acceleration fits to observed values, as well as the shear zone activation at the northern margin.

So far changes in ice shelf geometry have not been considered, which has to be done in future model runs.

References

Bamber, J.L. and P. Huybrechts. 1996. Geometric boundary conditions for modelling the velocity field of the Antarctic ice sheet. *Ann. Glaciol.* **23**, 364-373.

Lythe, M.B., D.G. Vaughan, and the BEDMAP Consortium. 2001. BEDMAP: A new ice thickness and subglacial topographic model of Antarctica. *J. Geophys. Res.* **106** (B6), 11,335-11,351.

Rack, W. 2000. Dynamic Behavior and Disintegration of the Northern Larsen Ice Shelf, Antarctic Peninsula, PhD-thesis, Univ. Innsbruck, Austria.

Rack, W., and H. Rott. Pattern of retreat and disintegration of Larsen B Ice Shelf, Antarctic Peninsula. Ann. Glaciol. 39, in press.

Sandhäger, H. 2000. Quantifizierung eisdynamischer und massenhaushaltsrelevanter Basisgrößen eines antarktischen Inlandeis-Schelfeis-Systems unter Einsatz eines numerischen Fließmodells. PhD-thesis, Univ. Münster, Germany.

Sandhäger, H. in press. Numerical study on the influence of fractures and zones of weakness on the flow regime of Larsen Ice Shelf. *FRISP* Report **14**. AWI Bremerhaven.

Vaughan, D.G. and C.S.M. Doake. 1996. Recent atmospheric warming and retreat of ice shelves on the Antarctic Peninsula. *Nature* **379**, 328-331.

Acknowledgements

The ERS data were made available by ESA through the VECTRA project, and the Envisat data through AO-ID308.